Journal of MATERIALS RESEARCH

Article
DOI: 10.1557/jmr.2019.360

A van der Waals contact-bond model for low-dimensional nanoscale carbon materials based on the quasi-continuum method

Xiangyang Wang[1,a)], Huibo Qi[1], Zhongyu Sun[1], Lifen Hu[1]

[1]School of Transportation, Ludong University, Yantai, Shandong 264025, China

[a)]Address all correspondence to this author. e-mail: wxy017@126.com

Received: 7 September 2019; accepted: 8 November 2019

In order to develop an efficient and accurate quasi-continuum approach for contact problems of low-dimensional nanoscale carbon materials, a van der Waals contact-bond model is proposed in this study. This method can involve the important information of nano- and micro-structures, such as the bonded carbon atom interactions and the long-range van der Waals effect, which is usually homogenized and neglected in continuum methods. The degree of freedom of the atomic systems can be reduced dramatically; therefore, the model is beneficial for rapid simulations and large-scale computations of carbon nano-components. The so-called higher-order Cauchy–Born rule is used to establish the geometrically consistent constitutive model, and a meshless local Petrov–Galerkin-based computational framework is constructed for the mechanical responses of carbon nanoscale systems. The stiffness matrix is derived analytically, and the incremental governing equation is solved with the Newton–Raphson iteration method. Consequently, this method is much faster than order-N^2 approaches such as molecular dynamic simulation.

Introduction

The study of the contact behaviors for low-dimensional nanoscale carbon materials and atomic systems, such as self-contact and interlayer contact, is of great technological and scientific interest. Numerous studies have been conducted on this important topic [1, 2, 3, 4, 5, 6, 7]. There are two main theoretical approaches to investigate the contact problems of carbon nanoscale structures, i.e., atomistic-based simulations and continuum mechanics methods. Both these methods, however, have the drawback of high computational complexity and, thus, demand unbearable amount of time when presenting numerical simulations for large-scale contact problems.

The atomistic-based approaches are developed for nanoscale problems which can easily take into account the interactions of bonded atoms and nonbonded atoms. However, they are not suitable for large-scale problems. The mechanical properties and responses of large systems cannot be predicted directly with the atomistic methods, and generally, the computational effort increases dramatically with the square of the system size. Consequently, atomistic-based simulations are limited to small-scale atomic systems [8, 9, 10, 11, 12]. Recently, Zhang and Tadmor [13, 14] proposed a discrete–continuum model for layered 2D materials which uses atomic simulation for short-range interactions and a continuum approximation for long-range interactions. This method can reduce the computational expense and capture the registry effects of stacked graphene sheets.

Extensive continuum mechanics models are developed for low-dimensional micro/nanoscale materials and systems [15, 16]. For conventional continuum methods, macroscopic material properties and responses are captured by constitutive models, which are phenomenological and obtained from experiments. For micro/nano-structures, in contrast, it is difficult to acquire accurate constitutive models from microscopic experiments for the continuum theoretical framework. As a result, the precision of the computations is generally lower than that of the atomistic simulations. One approach to tackle this problem is to use discrete elements, such as beams, rods, trusses, or springs, to represent the interatomic interactions of a pair of atoms to include the van der Waals (vdW) interactions [17, 18]. Although the nonlocal effect of multi-

https://doi.org/10.1557/jmr.2019.360 Published online by Cambridge University Press

© Materials Research Society 2019

body interactions of atoms can be taken into account, generally, the positions of the finite element nodes and atoms coincide with each other in these methods. Accordingly, these methods cannot reduce the degree of freedom of the system, and for large-scale problems, they require significant time. Another approach is the continuum cylindrical shell method. The computational efforts can be reduced significantly by decreasing the degree of freedom of the system. The nonlocal effect of the multi-body interactions of bonded atoms, however, cannot accurately be involved in this theory. And the interlayer interaction behaviors cannot be predicted precisely, especially for severe deformation, because the vdW interactions between discrete nonbonded atoms in different layers are homogenized on the equivalent continuum shell, and the total vdW energy of the system is obtained by integral operation over the whole domain [19, 20, 21, 22].

Recently, a few quasi-continuum (QC) methods are developed as multiscale methods that bridge the gap between discrete atomic structures and continuum solids. These methods are developing rapidly and have been successfully used to study the mechanical properties and responses of micro/nanoscale components, such as carbon nanotubes (CNTs) [23, 24, 25, 26], graphene [27], carbon nanocones [28], red blood cells [29], and microtubules [30]. The QC methods are of low cost and highly efficient, meaning that they are highly suitable for large-scale computations. The atomic structures are incorporated in the continuum theory via the homogeneous operation of the multi-body interatomic potential to obtain the continuum strain energy density. For example, Arroyo and Belytschko [31, 32, 33] combined the standard Cauchy–Born (CB) rule with the exponential map to develop an exponential CB rule for the linkage between the microscopic and macroscopic deformations and proposed a hyperelastic QC model for the investigation of mechanical properties of CNTs. On this basis, by involving vdW interactions between two contacted surfaces, the large deformations of CNTs considering contact are simulated numerically. Wang and Guo [34] proposed a contact model for the study of severe deformations of CNTs under thermal loading. Based on the proposed temperature-related higher-order Cauchy–Born (THCB) rule, the multiscale hyperelastic constitutive model was derived explicitly involving the nano-structural information of CNTs. Compared with molecular dynamic (MD) simulations, this method can reasonably avoid free surface intercutting with each other. It is noted that a double integral is performed for the calculation of the nonbonded energy, which results in high computational cost.

As mention above, compared with traditional continuum models, QC methods can almost achieve the accuracy of MD simulations since the important nanoscale information of discrete atomic structures and interatomic multi-body interactions can be reasonably incorporated into these constitutive models, i.e., the discreteness of nanoscale materials can be involved in the theory framework of the QC methods. Therefore, it is very important to reasonably consider the discreteness of nano-materials for the investigation of their mechanical properties. The research work of Gao and Klein [35] also confirms this point. They proposed a virtual internal bond model with randomized cohesive interactions between material particles as a combination of continuum models with cohesive surfaces and atomistic models with discrete atomic structures. With the use of the proposed method, they successfully studied strain localization problems of isotropic solids, such as crack initiation and growth.

Motivated by the virtual internal bond model proposed by Gao and Klein [35], we develop a van der Waals (vdW) contact-bond model, where the vdW interactions of nonbonded atoms in the atomic system are simulated by contact bonds between the evaluated points and nodes to take into account the discreteness of the nanoscale components. Compared with the atomistic-based simulations, the established vdW contact-bond model is more effective and efficient in predicting large deformations of nano-structures where the contact behaviors cannot be neglected. The amount of contact bonds can be selected freely for different contact problems. Besides, the computational efforts can, therefore, be significantly reduced, which is particularly attractive in engineering applications. In the higher-order QC model, the geometrically consistent higher-order Cauchy–Born (HCB) rule proposed by Guo et al. [23] is applied to construct the atomic-scale constitutive model. The HCB rule bridges the deformation between the atomic structures and the corresponding equivalent continuum membrane. Many successful applications of the QC model for graphene, nanotubes, nanocones, erythrocyte, microtubules, etc., can be found in Refs. [23, 24, 25, 26, 27, 28, 29, 30]. A variationally consistent meshless computational framework is established based on the developed vdW contact-bond QC model to predict the large deformation of nanoscale carbon components. The meshless local Petrov–Galerkin (MLPG) method [36, 37] is resorted to establish a numerical computational framework in which the displacement approximation has higher order continuity. It is a truly meshless method for interpolation and integration purposes, and no additional smoothing technique is required to evaluate the derivatives of the unknown variables.

Interactions between carbon atoms

The interactions between atoms in nanoscale carbon structures include multi-body interatomic potential and pair interatomic potential. Generally, the bond energy of the C–C covalent bond

https://doi.org/10.1557/jmr.2019.360 Published online by Cambridge University Press

© Materials Research Society 2019

can be described by the multi-body Tersoff–Brenner interatomic potential [38].

$$V(r_{IJ}) = V_{\mathrm{R}}(r_{IJ}) - \bar{B}_{IJ} V_{\mathrm{A}}(r_{IJ}) \quad , \tag{1}$$

where r_{IJ} denotes the distance between atoms I and J. V_{R} and V_{A} represent the repulsive and attractive pair terms, respectively. $\bar{B}_{IJ}$ represents the effect of multi-body coupling between bond I–J and other adjacent bonds emanating from atom I. In Eq. (1),

$$V_{\mathrm{R}}(r) = \frac{D^{(e)}}{S-1} \mathrm{e}^{-\sqrt{2S}\beta\left[r-R^{(e)}\right]} f_{\mathrm{c}}(r) \quad , \tag{2}$$

$$V_{\mathrm{A}}(r) = \frac{D^{(e)}}{S-1} S \mathrm{e}^{-\sqrt{2/S}\beta\left[r-R^{(e)}\right]} f_{\mathrm{c}}(r) \quad , \tag{3}$$

$$\bar{B}_{IJ} = \frac{1}{2}\left(B_{IJ} + B_{JI}\right) \tag{4}$$

with

$$B_{IJ} = \left[1 + \sum_{K(\neq I,J)} G(\theta_{IJK}) f_{\mathrm{c}}(r_{IK})\right]^{-\delta} \quad , \tag{5}$$

$$G(\theta) = a_0 \left[1 + \frac{c_0^2}{d_0^2} - \frac{c_0^2}{d_0^2 + (1+\cos\ \theta)^2}\right] \quad , \tag{6}$$

and θ_{IJK} represents the angle between bonds I–J and I–K. f_{c} is a smooth switch function to limit the range of the potential, whose form is usually taken as follows:

$$f_{\mathrm{c}}(r) = \begin{cases} 1 & r \le R^{(1)} \\ \frac{1}{2}\left\{1 + \cos\left(\frac{\pi\left(r - R^{(1)}\right)}{R^{(2)} - R^{(1)}}\right)\right\} & R^{(1)} < r \le R^{(2)} \\ 0 & r > R^{(2)} \end{cases} \quad . \tag{7}$$

In this study, the parameters in Eqs. (2)–(7) are set as [38]. $D^{(e)} = 6.000$ eV, $S = 1.22$, $\beta = 21$ nm^{-1}, $R^{(e)} = 0.1390$ nm, $\delta = 0.50000$, $a_0 = 0.00020813$, $c_0 = 330$, $d_0 = 3.5$, $R^{(1)} = 0.17$ nm, and $R^{(2)} = 0.20$ nm.

The vdW interatomic interactions between nonbonded carbon atoms can be represented by a pair interatomic potential such as the Lennard–Jones (LJ) potential [39].

$$V_{\mathrm{nb}} = 4\varepsilon\left[\left(\frac{\sigma}{r^{\mathrm{nb}}}\right)^{12} - \left(\frac{\sigma}{r^{\mathrm{nb}}}\right)^{6}\right] \quad , \tag{8}$$

where V_{nb} denotes the nonbonded energy between two nonbonded atoms. r^{nb} represents the distance between two nonbonded atoms. ε is the depth of the potential well. σ is the equilibrium distance at which the interatomic interaction potential is zero. In the present study, the values of parameters ε and σ are taken as 2.39 meV and 0.34 nm [40], respectively.

The vdW contact-bond model

The constitutive relationship

Compared with the classical CB rule, the HCB rule proposed by Guo et al. [23] for low-dimensional nanocrystalline membranes can enable the mapping of the atomic bonds more accurately. It can account of the curvature effect, which is important for crystalline membranes, in a geometrically consistent way since it involves the second-order or an even more higher-order deformation gradient tensor. The QC constitutive models can involve the information of pair and multi-body interactions of discrete atoms via the HCB rule as an atomic-continuum linkage. Consequently, the HCB rule is appropriate to construct a multiscale QC model for micro/nanoscale materials, including both microstructures and continuum solids. Many studies have shown that the HCB rule, which pulls the membranes more close to the real deformed configurations, can avoid severe numerical instabilities, such as spurious wrinkling [25, 26, 27, 28, 29]. The HCB rule can be written as

$$\boldsymbol{r} = \boldsymbol{F}\cdot\boldsymbol{R} + \frac{1}{2}\boldsymbol{G} : (\boldsymbol{R}\otimes\boldsymbol{R}) \quad , \tag{9}$$

where $\boldsymbol{r}$ and $\boldsymbol{R}$ denote the lattice vectors in the deformed and undeformed configurations, respectively. $\boldsymbol{F}$ and $\boldsymbol{G} = \nabla\boldsymbol{F}$ are the first- and second-order deformation gradient tensors, respectively, which can be defined by

$$\boldsymbol{F} = \frac{\partial \boldsymbol{x}}{\partial \boldsymbol{X}}, \quad \boldsymbol{G} = \frac{\partial^2 \boldsymbol{x}}{\partial \boldsymbol{X}\otimes\partial \boldsymbol{X}} \quad , \tag{10}$$

where $\boldsymbol{X} = (X_1, X_2)^T$ is the material coordinate of a point in the reference configuration (i.e., the planar graphene sheet) and $\boldsymbol{x} = (x_1, x_2, x_3)^T$ is the image of $\boldsymbol{X}$ in the current configuration. Since the hexagonal crystal lattice of graphene is not centrosymmetrical, in order to guarantee the inner equilibrium of the nano-structure, an inner relaxation parameter $\boldsymbol{\eta}$ is introduced and the HCB rule is rewritten as

$$\boldsymbol{r} = \boldsymbol{F}\cdot(\boldsymbol{R}+\boldsymbol{\eta}) + \frac{1}{2}\boldsymbol{G} : [(\boldsymbol{R}+\boldsymbol{\eta})\otimes(\boldsymbol{R}+\boldsymbol{\eta})] \quad , \tag{11}$$

where $\boldsymbol{\eta} = (\eta_1, \eta_1)^T$ can be obtained from the energy minimization with respect to $\boldsymbol{\eta}$ [23].

The strain energy density W_0 of continuum carbon components can be defined as

$$W_0 = \frac{\sum_{J=1}^{3} V(\boldsymbol{r}_{IJ}, \boldsymbol{r}_{IK}, \theta_{IJK}, K \neq I, J)}{2\Omega_I} = W_0(\boldsymbol{F}, \boldsymbol{G}, \boldsymbol{\eta}(\boldsymbol{F}, \boldsymbol{G})) \quad , \tag{12}$$

where V is the Tersoff–Brenner potential energy stored in the representative cell, and Ω_I is the average area of atom I in the reference configuration (see Fig. 1 for reference).

From Eq. (12), the first Piola–Kirchhoff stress tensor $\boldsymbol{P}$ and the higher-order stress tensor $\boldsymbol{Q}$ can be derived as

https://doi.org/10.1557/jmr.2019.360 Published online by Cambridge University Press

© Materials Research Society 2019

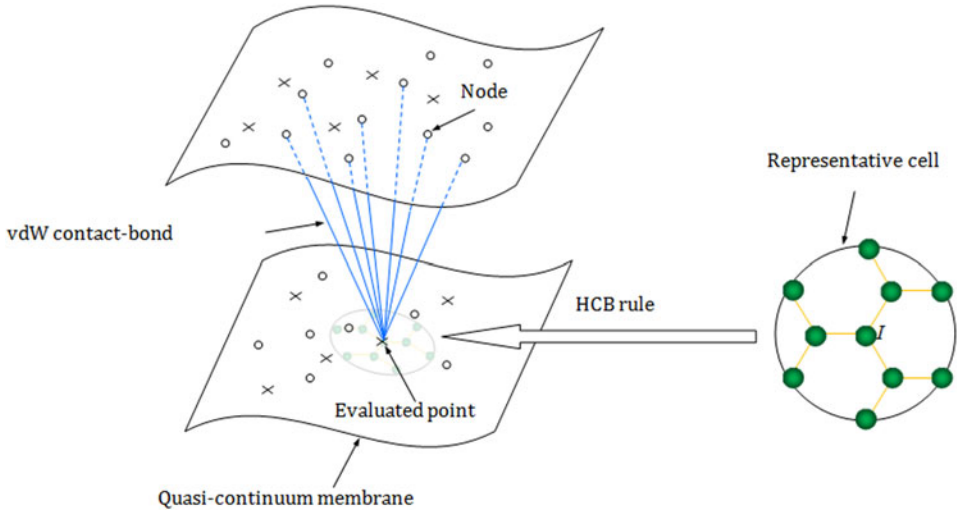


Figure 1: Illustration of the surface–surface interaction for the wall of CNTs.

$$\boldsymbol{P} = \frac{\partial W_0}{\partial \boldsymbol{F}} \quad , \tag{13}$$

$$\boldsymbol{Q} = \frac{\partial W_0}{\partial \boldsymbol{G}} \quad . \tag{14}$$

Since

$$\frac{\partial^2 W_0}{\partial \boldsymbol{\eta} \otimes \partial \boldsymbol{F}} + \frac{\partial^2 W_0}{\partial \boldsymbol{\eta} \otimes \partial \boldsymbol{\eta}} \cdot \frac{\partial \boldsymbol{\eta}}{\partial \boldsymbol{F}} = 0 \quad , \tag{15}$$

the tangent modulus tensors can be given as follows:

$$\boldsymbol{M}^{\mathrm{FF}} = \left.\frac{\partial^2 W_0}{\partial \boldsymbol{F} \otimes \partial \boldsymbol{F}}\right|_{\boldsymbol{\eta}=\hat{\boldsymbol{\eta}}} - \left.\left[\frac{\partial^2 W_0}{\partial \boldsymbol{F} \otimes \partial \boldsymbol{\eta}} \cdot \left(\frac{\partial^2 W_0}{\partial \boldsymbol{\eta} \otimes \partial \boldsymbol{\eta}}\right)^{-1} \cdot \frac{\partial^2 W_0}{\partial \boldsymbol{\eta} \otimes \partial \boldsymbol{F}}\right]\right|_{\boldsymbol{\eta}=\hat{\boldsymbol{\eta}}} , \tag{16}$$

$$\boldsymbol{M}^{\mathrm{FG}} = \left.\frac{\partial^2 W_0}{\partial \boldsymbol{F} \otimes \partial \boldsymbol{G}}\right|_{\boldsymbol{\eta}=\hat{\boldsymbol{\eta}}} - \left.\left[\frac{\partial^2 W_0}{\partial \boldsymbol{F} \otimes \partial \boldsymbol{\eta}} \cdot \left(\frac{\partial^2 W_0}{\partial \boldsymbol{\eta} \otimes \partial \boldsymbol{\eta}}\right)^{-1} \cdot \frac{\partial^2 W_0}{\partial \boldsymbol{\eta} \otimes \partial G}\right]\right|_{\boldsymbol{\eta}=\hat{\boldsymbol{\eta}}} , \tag{17}$$

$$\boldsymbol{M}^{\mathrm{GF}} = \left.\frac{\partial^2 W_0}{\partial \boldsymbol{G} \otimes \partial \boldsymbol{F}}\right|_{\boldsymbol{\eta}=\hat{\boldsymbol{\eta}}} - \left.\left[\frac{\partial^2 W_0}{\partial \boldsymbol{G} \otimes \partial \boldsymbol{\eta}} \cdot \left(\frac{\partial^2 W_0}{\partial \boldsymbol{\eta} \otimes \partial \boldsymbol{\eta}}\right)^{-1} \cdot \frac{\partial^2 W_0}{\partial \boldsymbol{\eta} \otimes \partial \boldsymbol{F}}\right]\right|_{\boldsymbol{\eta}=\hat{\boldsymbol{\eta}}} . \tag{18}$$

$$\boldsymbol{M}^{\mathrm{GG}} = \left.\frac{\partial^2 W_0}{\partial \boldsymbol{G} \otimes \partial \boldsymbol{G}}\right|_{\boldsymbol{\eta}=\hat{\boldsymbol{\eta}}} - \left.\left[\frac{\partial^2 W_0}{\partial \boldsymbol{G} \otimes \partial \boldsymbol{\eta}} \cdot \left(\frac{\partial^2 W_0}{\partial \boldsymbol{\eta} \otimes \partial \boldsymbol{\eta}}\right)^{-1} \cdot \frac{\partial^2 W_0}{\partial \boldsymbol{\eta} \otimes \partial \boldsymbol{G}}\right]\right|_{\boldsymbol{\eta}=\hat{\boldsymbol{\eta}}} , \tag{19}$$

where $\hat{\boldsymbol{\eta}}$ is the equilibrium solution of $\boldsymbol{\eta}$ given by

$$\frac{\partial W_0}{\partial \boldsymbol{\eta}} = 0 \quad . \tag{20}$$

For explicit expressions of the terms in the above equations, interested readers can refer to Guo et al. [23].

The vdW contact-bond model for point–surface contact

In this section, the vdW contact-bond model is proposed in the higher-order QC theoretical framework for the contact problems of a single carbon atom with a graphene sheet. In order to take into account the discreteness of the interactions of non-bonded atoms in the context of the QC method, the positions of atoms in the discrete nanoscale structure is equivalently replaced by the positions of nodes scattered on the surface of the continuum counterpart. The pair potential energy is assumed to be stored in the virtual bond between two neighbor nodes. A multiscale QC method based on the HCB rule is developed for low-dimensional nanoscale carbon components, and the information of atomic structures can be taken into account via the HCB rule.

The van der Waals (vdW) interaction between a single carbon atom $\bar{y}$ and a square graphene sheet is characterized by the LJ pair potential. The equivalent QC membrane for this atomistic system is divided by n discrete nodes independent of the number of carbon atoms, and the vdW energy V_{nb} of the system is given by

$$V_{\mathrm{nb}}\left(r^{\mathrm{nb}}\right) = 4\kappa_0 \varepsilon \sum_{I=1}^{\mathrm{v}} \left[\left(\frac{\sigma}{r_I^{\mathrm{nb}}}\right)^{12} - \left(\frac{\sigma}{r_I^{\mathrm{nb}}}\right)^{6}\right] \quad , \tag{21}$$

where the parameter $\kappa_0 = \frac{A_0}{\Omega_0}$, in which A_0 denotes the area occupied by a node in the QC membrane and Ω_0 represents the area divided up evenly to an atom in the graphene sheet. r_I^{nb} is the I-th vdW contact-bond length which can be described as a function of the position of node I, i.e., $r_I^{\mathrm{nb}} = |\boldsymbol{x}_I - \bar{y}|$, where $\boldsymbol{x}_I = (x_{I1}, x_{I2}, x_{I3})^T$ and $\bar{y} = (\bar{y}_1, \bar{y}_2, \bar{y}_3)^T$ is the position of the single atom. $n \leq N$ represents the number of contact bonds, which can be chosen freely based on the particularity of problems, such as for the case that the distance of the vdW

https://doi.org/10.1557/jmr.2019.360 Published online by Cambridge University Press

© Materials Research Society 2019

interaction is relatively large (≥0.85 nm), and n is taken as zero.

The total energy of the atomic system can be written as

$$E_{\text{tot}} = V_{\text{int}} + V_{\text{nb}} + V_{\text{ext}} \quad , \tag{22}$$

where

$$V_{\text{int}} = \int_{\Omega} W_0(\boldsymbol{F}, \boldsymbol{G}) \mathrm{d}\Omega \tag{23}$$

is the internal energy of the QC membrane obtained via the HCB rule as the bridge of the deformation between the atomic structure and the equivalent continuum membrane, and

$$V_{\text{ext}} = -\int_{\Omega} \boldsymbol{b}_0 \cdot \boldsymbol{u} \mathrm{d}\Omega - \int_{\Gamma_t} \boldsymbol{t}_0^P \cdot \boldsymbol{u} \mathrm{d}S - \int_{\Gamma_t} \boldsymbol{t}_0^Q \cdot \nabla_N \boldsymbol{u} \mathrm{d}S \tag{24}$$

is the external potential (if there is any) of the body force density $\boldsymbol{b}_0$, boundary traction $\boldsymbol{t}_0^P$, and boundary couple t_0^Q.

The equilibrium configuration of solids corresponds to a state of energy minimization, which can be described by the consistent variation of the E_{tot} in Eq. (22) with respect to displacement $\boldsymbol{u}$ as

$$\delta E_{\text{tot}}(\boldsymbol{u}; \delta\boldsymbol{u}) = \delta V_{\text{int}}(\boldsymbol{u}; \delta\boldsymbol{u}) + \delta V_{\text{nb}}(\boldsymbol{u}; \delta\boldsymbol{u}) + \delta V_{\text{ext}}(\delta\boldsymbol{u}) = 0 \quad , \tag{25}$$

with the condition $\delta^2 E_{\text{tot}} > 0$. In the continuum meshless numerical framework, $\boldsymbol{u}$ can be interpolated by the moving least square (MLS) approximation [41] as

$$\boldsymbol{u} = \sum_{I=1}^{N} \phi_I(\boldsymbol{X}) \boldsymbol{u}_I^* \quad , \tag{26}$$

where N is the total number of nodes in the influence domain, $\boldsymbol{u}_I^*$ denotes the displacement parameter of the I-th node, and $\phi_I(\boldsymbol{X})$ is the corresponding meshless shape function, which is expressed by

$$\phi_I(\boldsymbol{X}) = \boldsymbol{p}(\boldsymbol{X}) \cdot \left[\boldsymbol{A}^{-1}(\boldsymbol{X}) \cdot \boldsymbol{B}(\boldsymbol{X})\right]_I \quad , \tag{27}$$

in which $\boldsymbol{p}(\boldsymbol{X})$ is a full polynomial, and

$$\boldsymbol{A}(\boldsymbol{X}) = \sum_{I=1}^{N} \omega(\boldsymbol{X} - \boldsymbol{X}_I) \boldsymbol{p}(\boldsymbol{X}_I) \cdot \boldsymbol{p}(\boldsymbol{X}_I) \quad , \tag{28}$$

$$\boldsymbol{B}(\boldsymbol{X}) = [\omega(\boldsymbol{X} - \boldsymbol{X}_1)\boldsymbol{p}(\boldsymbol{X}_1),\ \omega(\boldsymbol{X} - \boldsymbol{X}_2)\boldsymbol{p}(\boldsymbol{X}_2), \ldots, \omega(\boldsymbol{X} - \boldsymbol{X}_N)\boldsymbol{p}(\boldsymbol{X}_N)] \quad , \tag{29}$$

where $\omega(\boldsymbol{X} - \boldsymbol{X}_I)$ is the weight function; in this study, the cubic spline function is used as ω.

This carbon atomic system is nonlinear in nature; by substituting Eq. (26) into Eq. (25) and linearizing this virtual work representation, it yields the following incremental governing equation:

$$\boldsymbol{K}(\boldsymbol{u}^n)\Delta\boldsymbol{u} = \boldsymbol{f}(\boldsymbol{u}^n) \quad , \tag{30}$$

where $\boldsymbol{u}^n$ denotes the displacement of the n-th step iteration, $\Delta\boldsymbol{u}$ represents the displacement increment, $\boldsymbol{K}$ is the stiffness matrix given by

$$K_{\alpha i \beta j} = \frac{\partial^2 V_{\text{int}}}{\partial u_{\alpha i}^* \partial u_{\beta j}^*} + \frac{\partial^2 V_{\text{nb}}}{\partial u_{\alpha i}^* \partial u_{\beta j}^*} \quad , \tag{31}$$

and $\boldsymbol{f}$ is the nonequilibrium force vector given by

$$f_{\alpha i} = -\frac{\partial V_{\text{int}}}{\partial u_{\alpha i}^*} - \frac{\partial V_{\text{nb}}}{\partial u_{\alpha i}^*} - \frac{\partial V_{\text{ext}}}{\partial u_{\alpha i}^*} \quad , \tag{32}$$

in which

$$\frac{\partial^2 V_{\text{int}}}{\partial u_{\alpha i}^* \partial u_{\beta j}^*} = \int_{\Omega} M_{iKjL}^{\text{FF}} \phi_{\alpha,K} \phi_{\beta,L} + M_{iKjLM}^{\text{FG}} \phi_{\alpha,K} \phi_{\beta,LM} + M_{iKLjM}^{\text{GF}} \phi_{\alpha,KL} \phi_{\beta,M} + M_{iKLjMN}^{\text{GG}} \phi_{\alpha,KL} \phi_{\beta,MN} \mathrm{d}\Omega \quad , \tag{33}$$

$$\frac{\partial^2 V_{\text{nb}}}{\partial u_{\alpha i}^* \partial u_{\beta j}^*} = \sum_{I=1}^{n} \left\{ V_{\text{nb}}''(|\boldsymbol{x} - \bar{\boldsymbol{y}}|_I) \frac{1}{\langle \boldsymbol{x} - \bar{\boldsymbol{y}} | \boldsymbol{x} - \bar{\boldsymbol{y}} \rangle_I} \left((\varphi_i(\boldsymbol{X}) + u_i(\boldsymbol{X}))_I - \bar{y}_i \right) \left((\varphi_j(\boldsymbol{X}) + u_j(\boldsymbol{X}))_I - \bar{y}_j \right) \phi_\alpha(\boldsymbol{X}) \phi_\beta(\boldsymbol{X}) + V_{\text{nb}}'(|\boldsymbol{x} - \bar{\boldsymbol{y}}|_I) \left\{ -\frac{1}{2} \frac{1}{\langle \boldsymbol{x} - \bar{\boldsymbol{y}} | \boldsymbol{x} - \boldsymbol{y} \rangle_I^{\frac{3}{2}}} \left((\varphi_i(\boldsymbol{X}) + u_i(\boldsymbol{X}))_I - \bar{y}_i \right) \left((\varphi_j(\boldsymbol{X}) + u_j(\boldsymbol{X}))_I - \bar{y}_j \right) \phi_\alpha(\boldsymbol{X}) \phi_\beta(\boldsymbol{X}) + \frac{\delta_{ij} \phi_\alpha(\boldsymbol{X}) \phi_\beta(\boldsymbol{X})}{|\boldsymbol{x} - \bar{\boldsymbol{y}}|_I} \right\} \right\} \quad , \tag{34}$$

$$\frac{\partial V_{\text{int}}}{\partial u_{\alpha i}^*} = \int_{\Omega} P_{iM} \phi_{\alpha,M} + Q_{iMN} \phi_{\alpha,MN} \mathrm{d}\Omega \quad , \tag{35}$$

$$\frac{\partial V_{\text{nb}}}{\partial u_{\alpha i}^*} = \sum_{I=1}^{n} \left(V_{\text{nb}}'(|\boldsymbol{x} - \bar{\boldsymbol{y}}|_I) \frac{1}{|\boldsymbol{x} - \bar{\boldsymbol{y}}|_I} \left((\varphi_i(\boldsymbol{X}) + u_i(\boldsymbol{X}))_I - \bar{y}_i \right) \phi_\alpha(\boldsymbol{X}) \right) \quad , \tag{36}$$

$$\frac{\partial V_{\text{ext}}}{\partial u_{\alpha i}^*} = \int_{\Omega} b_{0i} \phi_\alpha d\Omega + \int_{\Gamma_t} t_{0i}^P \phi_\alpha + t_{0i}^Q N_M \phi_{\alpha,M} \mathrm{d}S \quad , \tag{37}$$

where φ is the mapping from the graphene sheet to the undeformed nanotube.

The vdW contact-bond model for surface–surface contact

The vdW contact-bond model for surface–surface contact problems has higher complexity than the model proposed earlier for the point–surface contact. The vdW interactions of two adjacent carbon crystalline membranes are shown in Fig. 1. The vdW energy V_{nb} between an evaluated point and discrete nodes is given as

https://doi.org/10.1557/jmr.2019.360 Published online by Cambridge University Press

© Materials Research Society 2019

$$V_{\mathrm{nb}}\left(r^{\mathrm{nb}}\right)=4\kappa_0\kappa_1\varepsilon\sum_{I=1}^{n}\left[\left(\frac{\sigma}{r_I^{\mathrm{nb}}}\right)^{12}-\left(\frac{\sigma}{r_I^{\mathrm{nb}}}\right)^{6}\right] \quad , \qquad (38)$$

where $\kappa_1=\frac{A_1}{\Omega_0}$, in which A_1 is the area occupied by the evaluated point, such as the Gaussian quadrature point for the meshless numerical simulation in the following section. The total vdW energy of the system via Eq. (38) is

$$V_{\mathrm{nb}}^{\mathrm{tot}}=\frac{1}{2}\int_{\Omega}\frac{V_{\mathrm{nb}}\left(r^{\mathrm{nb}}\right)}{\Omega_0}\mathrm{d}V \quad . \qquad (39)$$

As shown in the following calculations, a small number of contact bonds can guarantee the accuracy of the numerical simulation. It is, therefore, much faster than other existing continuum methods where the vdW energy is represented by [33, 34].

$$V_{\mathrm{nb}}^{\mathrm{tot}}=\frac{1}{2}\int_{\Omega}\int_{\Omega}\frac{V_{\mathrm{nb}}\left(r^{\mathrm{nb}}\right)}{\Omega_0^2}\mathrm{d}V\mathrm{d}V \quad . \qquad (40)$$

It is a double integral function, and the computation requires a double loop over the domain Ω. Its numerical computational effort increases with the square of the system size such that these continuum methods are not suitable for large-scale atomic systems.

The vdW interactions depend only on the distance between discrete atoms, which are replaced by single nodes in the contact-bond model. Unlike the homogenization operation of vdW interactions in the continuum methods, the interactions between discrete evaluated points (nodes/quadrature points) in one film and those in another film are described exactly, which ensures the accuracy of this method. Contrary to the atomistic simulations, the proposed contact-bond–based QC method can significantly reduce the degree of freedom of the components and decrease the computation scale, which enables rapid evaluation of large-scale problems.

The first- and second-order derivatives of the vdW energy in Eq. (39) with respect to displacement $\boldsymbol{u}$ for a nonequivalent force vector and stiffness matrix in the governing Eq. (21), respectively, are

$$\frac{\partial V_{\mathrm{nb}}^{\mathrm{tot}}}{\partial u_{ai}^{*}}=\frac{1}{2}\int_{\Omega}\frac{1}{\Omega_0}\sum_{I=1}^{n}\left(V_{\mathrm{nb}}^{'}\left(|x-\bar{y}|_I\right)\frac{1}{|x-\bar{y}|_I}\right.$$

$$\left.\left(\left(\varphi_i(X)+u_i(X)\right)_I-\bar{y}_{iI}\right)\phi_\alpha(X)\right)\mathrm{d}V$$

$$=\frac{1}{2}\frac{1}{\Omega_0}\sum_{e=1}^{N}\sum_{k=1}^{gus}\sum_{I=1}^{n}\left(V_{\mathrm{nb}}^{'}\left(|x_k-\bar{y}|_I\right)\frac{1}{|x_k-\bar{y}|_I}\right.$$

$$\left.\left(\left(\varphi_i(X)+u_i(X)\right)_{kI}-\bar{y}_{iI}\right).\left(\phi_\alpha(X)\right)_k\right)|J(X)^e|w_i^e(X) \quad , \qquad (41)$$

$$\frac{\partial^2 V_{\mathrm{nb}}^{\mathrm{tot}}}{\partial u_{\alpha i}^{*}\partial u_{\beta j}^{*}}=\frac{1}{2}\frac{1}{\Omega_0}\int_{\Omega}\sum_{I=1}^{n}\left[V_{\mathrm{nb}}^{''}\left(|x-\bar{y}|_I\right)\frac{1}{\langle x-y|x-y\rangle_I}\right.$$

$$\left(\left(\varphi_i(X)+u_i(X)\right)_I-\bar{y}_{iI}\right)\left(\left(\varphi_j(X)+u_j(X)\right)_I-\bar{y}_{jI}\right)$$

$$\left.\boldsymbol{\phi}_\alpha(X)\boldsymbol{\phi}_\beta(X)\right]+\sum_{I=1}^{n}\left\{V_{nb}^{'}\left(|x-\bar{y}|_I\right)\right.$$

$$\left\{\left[-\frac{1}{2}\frac{1}{\left(\langle x-\bar{y}|x-\bar{y}\rangle_I\right)^{\frac{3}{2}}}\left(\left(\varphi_i(X)+u_i(X)\right)_I-\bar{y}_{iI}\right)\right.\right.$$

$$\left.\left.\left(\left(\varphi_j(X)+u_j(X)\right)_I-\bar{y}_{jI}\right)\boldsymbol{\phi}_\alpha(X)\boldsymbol{\phi}_\beta(X)\right]+\frac{\delta_{ij}\boldsymbol{\phi}_\alpha(X)\boldsymbol{\phi}_\beta(X)}{|x-\bar{y}|_I}\right\}\right\}\mathrm{d}V$$

$$=\frac{1}{2}\frac{1}{\Omega_0}\sum_{e=1}^{N}\sum_{k=1}^{gus}\sum_{I=1}^{n}\left\{\left[V_{\mathrm{nb}}^{''}\left(|x_k-\bar{y}|_I\right)\frac{1}{\langle\boldsymbol{x}_k-\bar{\boldsymbol{y}}|\boldsymbol{x}_k-\bar{\boldsymbol{y}}\rangle_I}\right.\right.$$

$$\left(\left(\varphi_i(\boldsymbol{X})+u_i(\boldsymbol{X})\right)_{kI}-\bar{y}_{iI}\right)\left(\left(\varphi_j(\boldsymbol{X})+u_j(\boldsymbol{X})\right)_{kI}-\bar{y}_{jI}\right)$$

$$\left.\left(\boldsymbol{\phi}_\alpha(\boldsymbol{X})\right)_k\left(\boldsymbol{\phi}_\beta(\boldsymbol{X})\right)_k\right]+V_{\mathrm{nb}}^{'}\left(|\boldsymbol{x}_k-\bar{\boldsymbol{y}}|_I\right)$$

$$\left\{-\frac{1}{2}\frac{1}{\left(\langle\boldsymbol{x}_k-\bar{\boldsymbol{y}}|\boldsymbol{x}_k-\bar{\boldsymbol{y}}\rangle_I\right)^{\frac{3}{2}}}\left(\left(\varphi_i(\boldsymbol{X})+u_i(\boldsymbol{X})\right)_{kI}-\bar{y}_{iI}\right)\right.$$

$$\left(\left(\varphi_j(\boldsymbol{X})+u_j(\boldsymbol{X})\right)_{kI}-\bar{y}_{jI}\right)\left(\boldsymbol{\phi}_\alpha(\boldsymbol{X})\right)_k\left(\boldsymbol{\phi}_\beta(\boldsymbol{X})\right)_k$$

$$\left.\left.+\frac{\delta_{ij}\left(\boldsymbol{\phi}_\alpha(\boldsymbol{X})\right)_k\left(\phi_\beta(\boldsymbol{X})\right)_k}{|\boldsymbol{x}_k-\bar{\boldsymbol{y}}|_I}\right\}\right\}|J(\boldsymbol{X})^e|w_i^e(\boldsymbol{X}) \quad , \qquad (42)$$

where N is the number of nodes, *gus* denotes the amount of Gaussian quadrature points within each local subdomain Ω_s in the following developed meshless computational framework, and n represents the number of contact bonds between adjacent quadrature points and nodes, which is far less than N, ensuring that the computation scale increases almost linearly with the system size N.

Meshless computational scheme

In recent years, the continuum meshless methods have come into a new stage of rapid development. Unlike the conventional finite element method, continuum solids are not divided into a finite number of elements (FEM), and the shape function depends on the discrete nodes in the local influence domain which overlaps with the neighbor ones in space. As a truly meshless method, the MLPG approach [36,

https://doi.org/10.1557/jmr.2019.360 Published online by Cambridge University Press

© Materials Research Society 2019

37] is naturally more efficient and flexible in dealing with nonlinear boundary value problems than the conventional FEM and element-free Galerkin (EFG) method. In this study, MLPG is applied to construct a meshless computational framework for the contact behaviors of low-dimensional carbon nano-structures. The degree of freedom of the system can be reduced significantly, and its computational efforts are much lower than those of molecular dynamics simulations. It is, therefore, suitable for the computations of technological applications.

As the proposed QC continuum approach for carbon nanoscale components is based on the Tersoff–Brenner potential, which is nonlinear in nature, the equilibrium configurations can be obtained by solving the linearized governing equation iteratively with the Newton–Raphson method. On the contrary, as the order-N^2 approaches involved only the first-order derivative of the total energy, such as the widely used conjugate gradient method in atomistic simulations, the proposed method enables rapid computations for large-scale systems and significantly reduces the computational efforts. It is noted that when nonlinear bifurcation or material softening occurs, the stiffness matrix K usually becomes nonpositive definite. Under this circumstance, the iterative solution converges to a spurious minimal energy state. This nonphysical problem can be remedied by the replacement of the nonpositive definite K with $K + \gamma I$, in which I is the same order identity matrix and γ is a positive number to ensure the positive definiteness of $K + \gamma I$ [18]. When the iterative solution approaches the real state of minimal energy, K recovers to positive definite.

The routine of the developed approach can be summarized as follows:

(i) Scatter a finite number of nodes in the domain Ω and on the boundary Γ of the system.
(ii) Determine the local sub-domain Ω_s and its boundary Γ_s for each node.
(iii) Loop over all local sub-domain Ω_s and Γ to calculate $\frac{\partial^2 V_{int}}{\partial u^* \otimes \partial u^*}$, $\frac{\partial V_{int}}{\partial u^*}$, and $\frac{\partial V_{ext}}{\partial u^*}$.
  (a) Determine the Gaussian points in Ω_s and on Γ_s.
  (b) Loop over all the Gaussian points.

(1) Calculate shape functions $\boldsymbol{\varphi}$ and their derivatives with respect to $\boldsymbol{X}$ via MLS approximation for the nodes in the influence domain of the Gaussianpoint.
(2) Calculate deformation gradient tensors $\boldsymbol{F}$ and $\boldsymbol{G}$.
(3) Calculate stress vectors $\boldsymbol{P}$ and $\boldsymbol{Q}$ and tangent modulus tensors $\boldsymbol{M}^{FF}$, $\boldsymbol{M}^{FG}$, $\boldsymbol{M}^{GF}$, and $\boldsymbol{M}^{GG}$.
(4) Assemble the contributions to $\boldsymbol{K}$ and $\boldsymbol{f}$.
  (c) End the Gaussian point loop.
(iv) End the domain and boundary loop.
(v) Loop over all local sub-domain Ω_s to calculate $\frac{\partial^2 V_{nb}}{\partial u^* \otimes \partial u^*}$ and $\frac{\partial V_{nb}}{\partial u^*}$.
  (a) Determine the Gaussian points in Ω_s.
  (b) Loop over all the Gaussian points.

(1) Calculate the r_{nb} with the use of the position of nodes obtained from the $(n-1)$-th iteration step.
(2) Calculate shape functions $\boldsymbol{\phi}$ via MLS approximation for the nodes in the influence domain of one node.
(3) Assemble the contributions to $\boldsymbol{K}$ and $\boldsymbol{f}$.
  (c) End the Gaussian point loop.
(vi) Solve the governing equation $K(u^n)\Delta u = f(u^n)$.
  (a) K is positive definite?
  (b) If no, then take K as $K + \gamma I$.
  (c) If yes, then continue.
(vii) Update the position of nodes.
(viii) Check if the convergence criterion is satisfied.
  (a) If no, then go to (iii).
  (b) If yes, then go to the next loading step.

From the above implementation, it is observed that this numerical approach is a truly meshless method without any elements used in conventional FEM and EFG. The nonlocal property of the shape function can readily satisfy the higher-order continuity requirement of the hyperelastic constitutive model for low-dimensional carbon nanoscale components based on the HCB rule.

Accuracy of the vdW contact-bond model

In this section, the accuracy and effectiveness of the vdW contact-bond model for low-dimensional carbon nanoscale contact problems are studied via the following contrast tests. In order to facilitate comparison, two simple examples are illustrated in Fig. 2, namely, point–face (PF) test [Fig. 2(a)] and point–point (PP) test [Fig. 2(b)], respectively. The single carbon atom is 0.6 nm above the 0.8 × 0.8-nm^2 square graphene sheet and descends gradually by 0.02 nm per step. The meshless nodes are uniformly scattered on the sheets. In order to exclude the influence of deformation of the graphene sheet for the vdW interactions, the graphene sheet is rigid and fixed. The discrete atomistic model

$$V_{nb} = 4\varepsilon \sum_{I=1}^{n} \left[\left(\frac{\sigma}{r_I^{nb}} \right)^{12} - \left(\frac{\sigma}{r_I^{nb}} \right)^{6} \right] , \qquad (43)$$

and the continuum method (homogenization treatment)

https://doi.org/10.1557/jmr.2019.360 Published online by Cambridge University Press

© Materials Research Society 2019

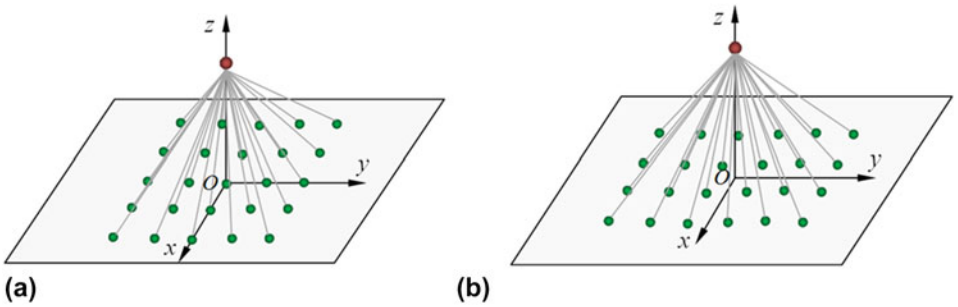


Figure 2: Schematic diagram of the point–surface interaction examples for the (a) PF test and (b) PP test, respectively.

$$V_{\mathrm{nb}} = \frac{1}{\Omega_0}\int_{-\frac{a}{2}}^{\frac{a}{2}}\int_{-\frac{a}{2}}^{\frac{a}{2}} 4\varepsilon\left(\left(\frac{\sigma}{\sqrt{x^2+y^2+z_{\mathrm{atom}}^2}}\right)^{12} - \left(\frac{\sigma}{\sqrt{x^2+y^2+z_{\mathrm{atom}}^2}}\right)^{6}\right)\mathrm{d}x\mathrm{d}y \qquad (44)$$

are taken for comparison, where a is the side length of the square graphene sheet, and z_{atom} represents the distance between the carbon atom and the origin of coordinates (square center).

Figure 3 shows the variations of the total vdW energy with respect to the distance between the discrete carbon atom and the graphene sheet for PP and PF tests, respectively, with the usage of the proposed contact-bond model, the atomistic calculation, and the continuum method. It is observed that the vdW energy decreases previously and increases later with the distance between the atom and the sheet reducing, and the turning points for both PP and PF tests appear around the distance of 0.3 nm (the atomistic simulation) and 0.32 nm (the contact-bond model and continuum method). Contrary to atomistic simulation, the continuum results both for PP and PF tests have severe deviation. Although our contact-bond model calculations somewhat underestimate the value of vdW energy when the distance is larger than about 0.26 nm (the vdW interaction is relatively weak), as long as the two components are extremely close, i.e., the distance is less than 0.26 nm, the simulation results of the contact-bond model are in good agreement with the atomistic calculations with an offset of approximately 10%, such as 6.1% for the PP test and 9.9% for the PF test as the distance reaches 0.1 nm.

The parameter κ_0 in Eq. (21) controlled by the number of meshless nodes has an influence on the vdW interactions simulation with the contact-bond–based QC method, and the results are given in Fig. 4. It is shown that the effect of κ_0 on the total vdW energy becomes significant when the distance between the discrete carbon atom and the graphene sheet is less than 0.2 nm. κ_0 has an increasing effect on the total vdW energy for the case of the PP test, but has a decreasing effect for the PF test. It can be seen that the value of κ_0 taken from about 1.0 to 1.5 can guarantee the consistency of our QC model with the atomistic method.

The influence of the number of contact bonds on the vdW interactions is also studied for the PF test, where $\kappa_0 = 1.327$, and the data are listed in Table I. It indicates that the 4 nearest-neighbor contact bonds play a major role in vdW interactions, and other next nearest-neighbor ones can be neglected, which is conductive to the rapid computation of large-scale systems.

From the above discussion, it is obviously observed that the proposed contact-bond model is as accurate as the atomistic simulation, since it involves the equivalently discrete nanostructures which cannot be accounted for in the continuum method. Moreover, the computational efforts can be reduced dramatically as fewer contact bonds are engaged, whereas the accuracy of computation is retained.

Numerical examples and discussion

In order to further demonstrate the proposed contact-bond model and the corresponding QC meshless scheme for the point–surface and surface–surface interactions of low-dimensional nanoscale carbon structures, three different examples are presented in this section.

The first example is for the point–surface contact problem of a single carbon atom and a square graphene sheet. Unlike the example used in the section "Accuracy of the vdW contact-bond model," only the four sides of a 4×4-nm^2 graphene sheet are fixed, and displacements of the rest of the domain are not restricted; i.e., the equilibrium configuration of the graphene sheet is determined via energy minimization with the use of the QC meshless scheme. 21×21 meshless nodes are used in this numerical simulation ($\kappa_0 = 1.37$).

Changes in the maximum deflections of the graphene sheet (the central point deflections) and the distances between the single carbon atom and the graphene sheet with respect to the displacement of the carbon atom are shown in Fig. 5(a). In the initial loading stage (the displacement decreases from 1.0 to 0.64 nm), the upward deflection of

https://doi.org/10.1557/jmr.2019.360 Published online by Cambridge University Press

© Materials Research Society 2019

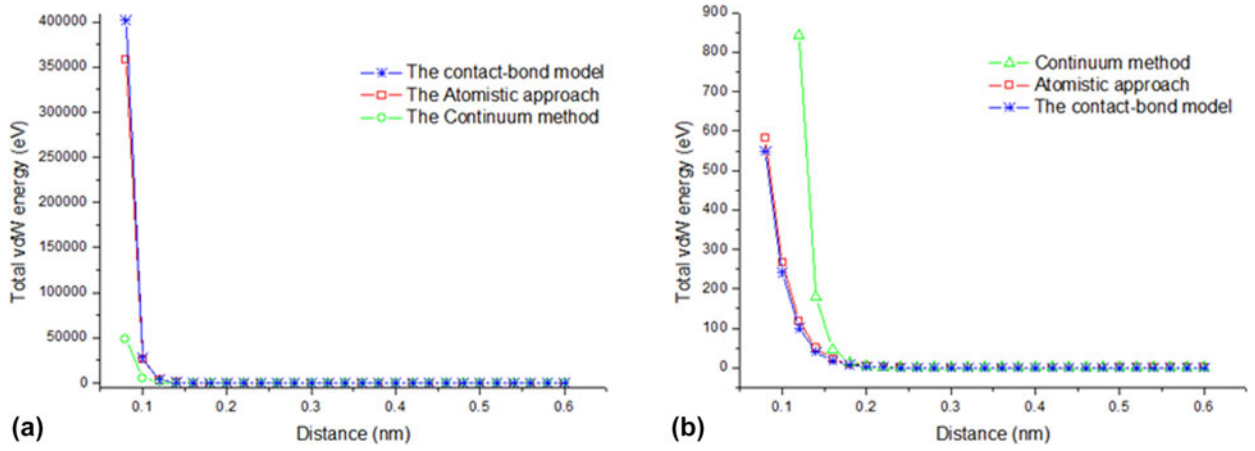


Figure 3: Variations of the total vdW energy with respect to the distance between the discrete carbon atom and the graphene sheet for the (a) PP test and (b) PF test, respectively.

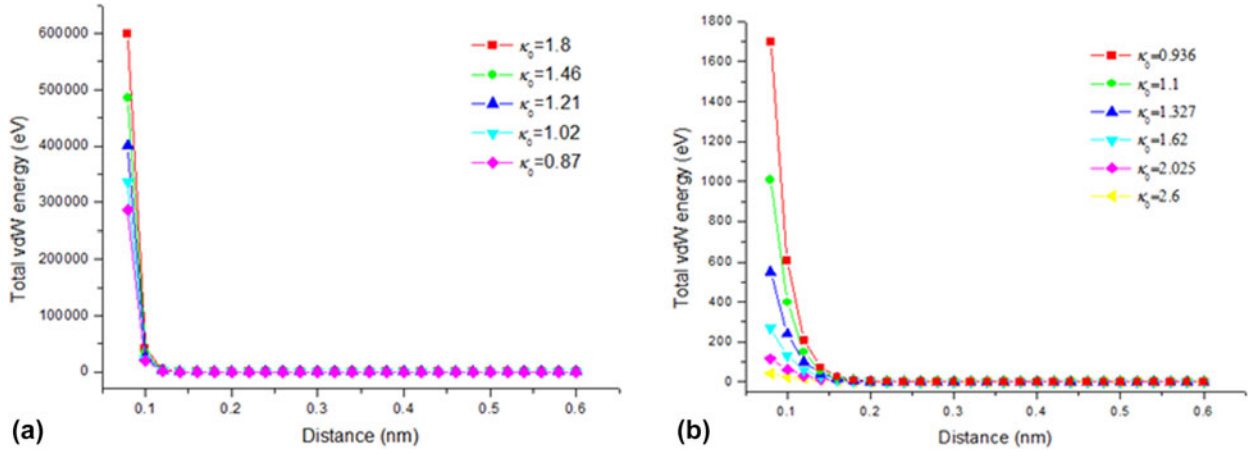


Figure 4: Influence of parameter κ_0 on the total vdW energy for the (a) PP test and (b) PF test.

TABLE I: Influence of the number of contact bonds on the total vdW energy ($\kappa_0 = 1.327$ for the PF test).

Distance (nm)	4 bonds	16 bonds	36 bonds	64 bonds
0.34	−0.01161	−0.02968	−0.0356	−0.03744
0.32	−0.00528	−0.02622	−0.03278	−0.03473
0.3	0.01373	−0.01025	−0.01748	−0.01955
0.28	0.06247	0.03545	0.0275	0.0253
0.26	0.18046	0.15075	0.14204	0.13972
0.24	0.46109	0.42956	0.42005	0.41761
0.22	1.12921	1.09747	1.08715	1.08459
0.2	2.73667	2.70741	2.69627	2.6936
0.18	6.65972	6.63697	6.62501	6.62222
0.16	16.3571	16.34635	16.33359	16.3307
0.14	40.45511	40.4632	40.44968	40.44669
0.12	99.73875	99.77327	99.75905	99.75597
0.1	240.38649	240.45463	240.43977	240.43661
0.08	549.21455	549.3213	549.30589	549.30267

the graphene sheet increases gradually, which is captured by the attraction of the vdW interaction. When the displacement is larger than 0.64 nm, the deformation of the graphene sheet is dominated by the repulsive interactions. The total vdW energy obtained from the PP test is larger than that from the PF test, as shown in Fig. 5(b). However, the resultant attractive force contributed by the nearest 4 nodes in the central portion of the graphene sheet in the PF test is larger than that of one node in the center of the graphene sheet in the PP test; the deflections [in Fig. 5(a)] and the strain energy per atom [in Fig. 5(c)] obtained from the PF test are slightly larger than those from the PP test as long as the distance between the atom and the graphene sheet is larger than 0.34 nm. Since the LJ potential increases dramatically when the distance $r^{nb} < 0.34$ nm, i.e., the distance has a tremendous effect on the vdW interaction (the repulsive interactions playing a dominant role), the contribution of the central node in the graphene sheet to its deflections and strain energy density is larger than that of the surrounding ones. Consequently, the deflections and strain energy density of the graphene sheet obtained in the PP test are larger than that given by the PF test.

https://doi.org/10.1557/jmr.2019.360 Published online by Cambridge University Press

© Materials Research Society 2019

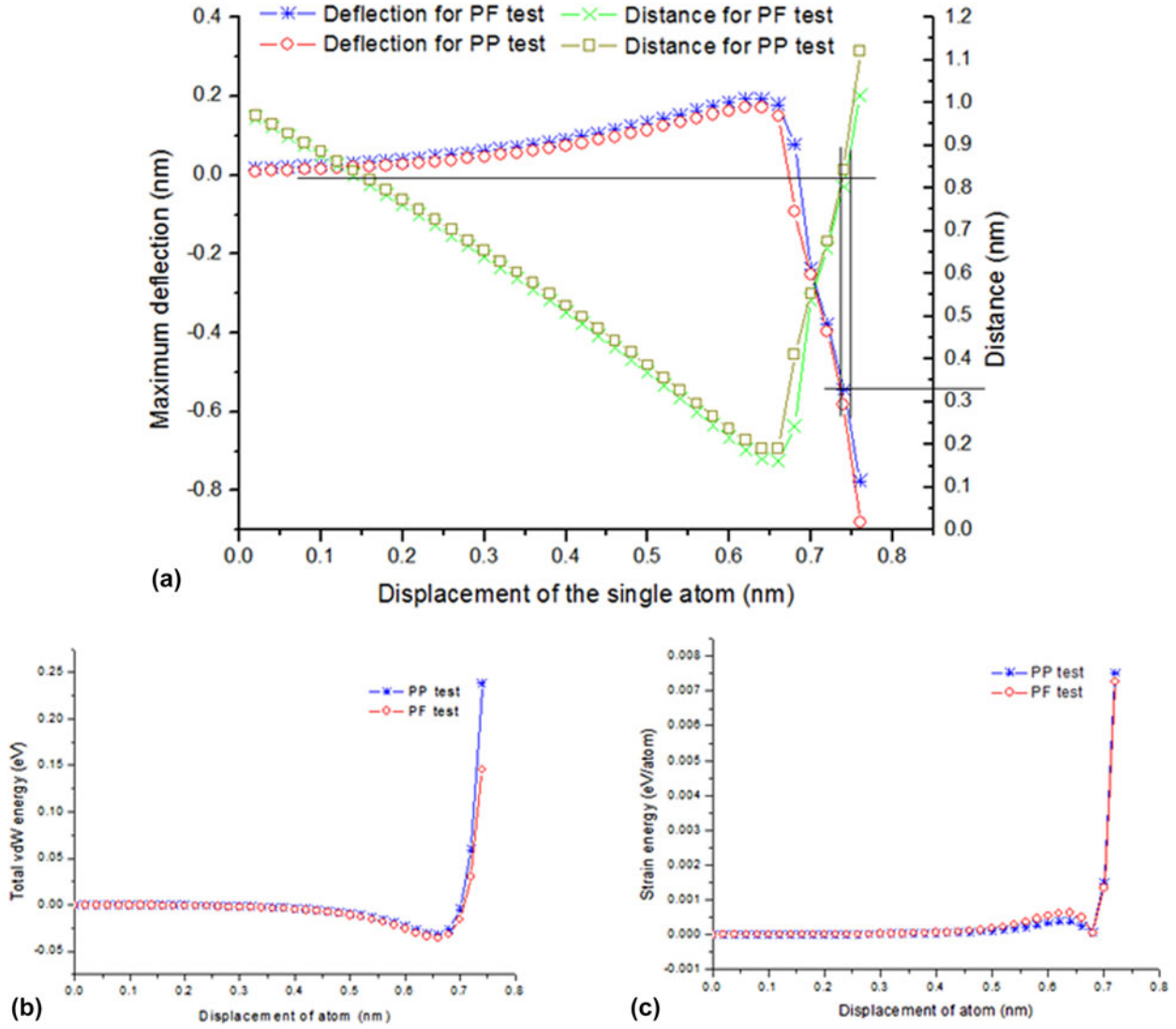


Figure 5: (a) Comparison for the maximum deflection of the graphene sheet as well as the distance between the single carbon atom and the graphene sheet under the displacement of the single carbon atom, and the variations of (b) the total vdW energy and (c) the strain energy of the graphene sheet with respect to the displacement of the single carbon atom under two types of loading.

From the above discussion, it is observed that carbon nanoscale point–surface interaction systems can be accurately studied with the proposed contact-bond model. The effectiveness of this method to calculate the nanoscale surface–surface problems for CNTs is illustrated in the following examples.

A (7,7) armchair CNT of 6 nm length is selected for the following examination. One end of the nanotube is fixed, and the other end is subjected to axial compression. The number of the meshless nodes is taken as 36 × 18. The variations in strain energy of the (7,7) CNT with respect to the axial compression strain are shown in Fig. 6. For the case of vdW interactions neglected, it can be observed that the first buckling of the SWCNT occurs at the critical strain of 0.062, and the second and third critical buckling strains are 0.09 and 0.105, respectively. This trend agrees well with those reported in [8] obtained from MD simulations. The corresponding buckling patterns are demonstrated in Figs. 7(a)–7(c). The effect of the vdW interactions on the response of the nanotube are presented in Figs. 6(b), 7(d), and (e). The disturbance due to vdW interactions changes the three-fan buckling pattern of the CNT to the two-fan mode and brings the post-buckling forward from the buckling strain of 0.105 to 0.07.

The twisting test of the (21,0) zigzag CNT is also carried out in this section. The tubular length is taken as 11.2 nm, and this nanotube includes 1890 carbon atoms. 58 × 24 meshless nodes are used in the QC meshless numerical simulation. The buckling patterns at different twisting angles are shown in Fig. 8 for the cases of with and without vdW interactions, respectively. From Fig. 8(a), it is observed that the middle portion of the nanotube becomes flat and starts to fold onto

https://doi.org/10.1557/jmr.2019.360 Published online by Cambridge University Press

© Materials Research Society 2019

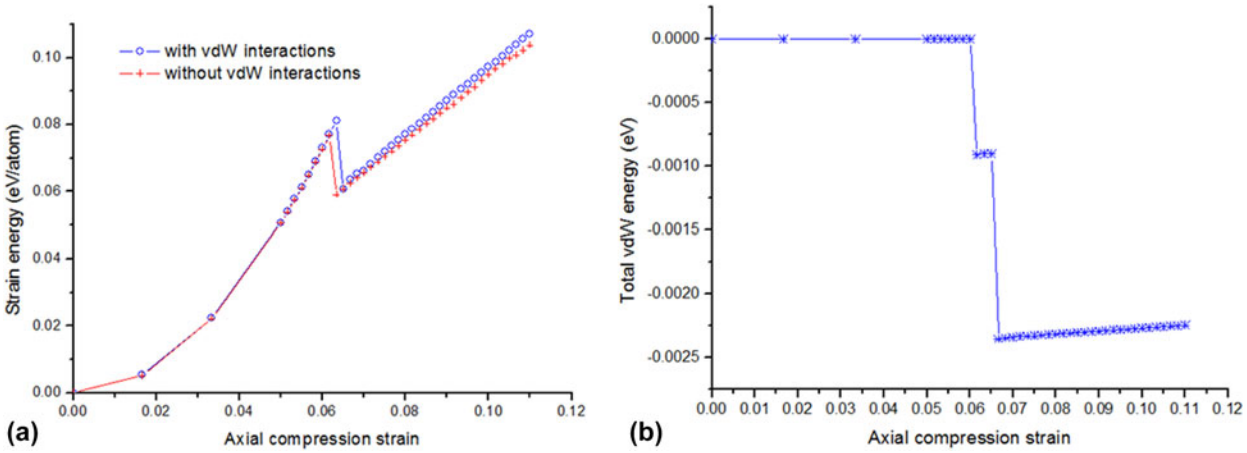


Figure 6: Changes in (a) the strain energy and (b) the total vdW energy for the CNT under compression with axial strain.

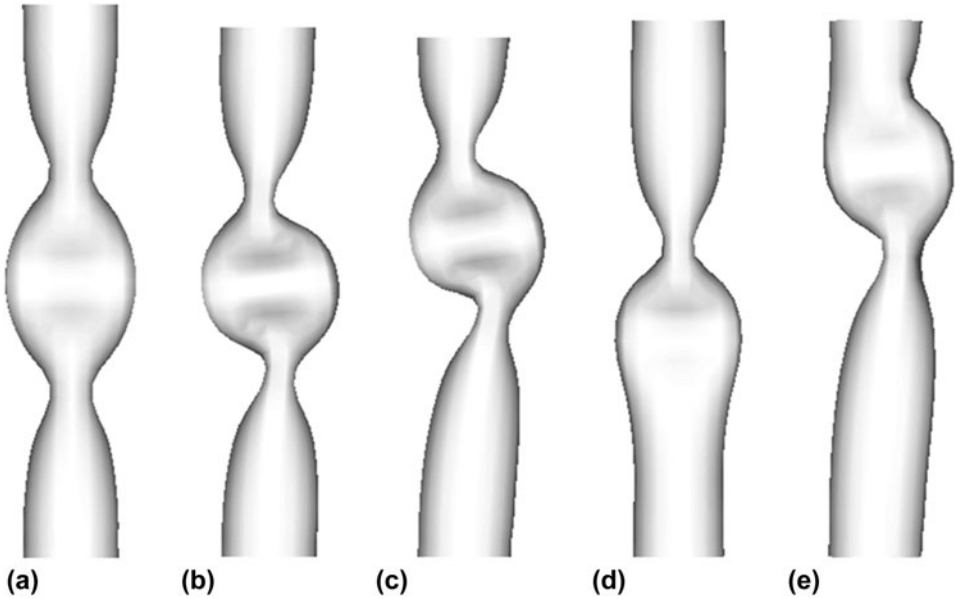


Figure 7: Compression buckling and post-buckling configurations of the (7, 7) CNT without involved vdW interactions at the critical strains of (a) 0.062, (b) 0.09, and (c) 0.105, as well as with involved vdW interactions at the critical strains of (d) 0.063 and (e) 0.07, respectively.

itself, which is in good agreement with those reported by Yakobson et al. [8] and Arroyo and Belytschko [33]. The buckling patterns without including the vdW interactions are displayed in Fig. 8(b). It can be seen that the deformation is unphysical and the wall of the nanotube has penetrated itself at a twisting angle of 70°. The computational efforts of this method are far less than that of our previous QC model which double searches the computational domain [34].

In order to further illustrate the effectiveness of the proposed method, a (6,0) (13,0) double-walled CNT with 5.08 nm length is selected for the numerical bending test. The buckling patterns at 23° bending angle are shown in Fig. 9. It can be seen that the inner tube is also buckling, which is effected by the outer tube through van der Waals interactions [Fig. 9(a)], which is in good agreement with that reported by Iijima et al. [42] and Arroyo and Belytschko [33]. By contrast, the inner tube is still unbuckling and penetrates the surface of the outer one at the same bending angle [Fig. 9(b)] without considering the contribution of the van der Waals interactions.

As a brief summary, the proposed contact-bond model and the corresponding meshless computational scheme are efficient and accurate for low-dimensional carbon nanoscale contact systems. The degree of freedom for the nanoscale components can be greatly reduced, thus saving the computational efforts. On the other hand, since the HCB rule, which is key to building the QC method, is not limited to a special atomistic model, our method can be expanded to other low-dimensional nanoscale components, such as BN, TiS_2, and MoS_2 nanotubes.

https://doi.org/10.1557/jmr.2019.360 Published online by Cambridge University Press

© Materials Research Society 2019

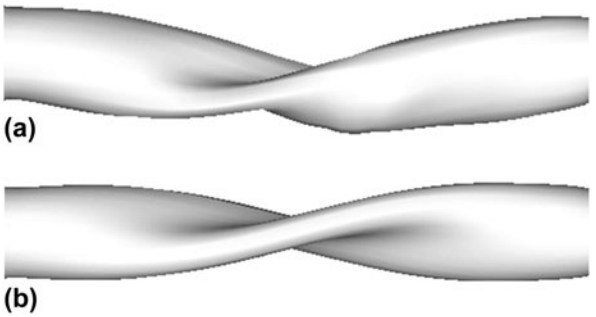


Figure 8: Torsional buckling configurations of the (21, 0) CNT (a) with involved vdW interactions and (b) without involved vdW interactions at the twist angle of 70°, respectively.

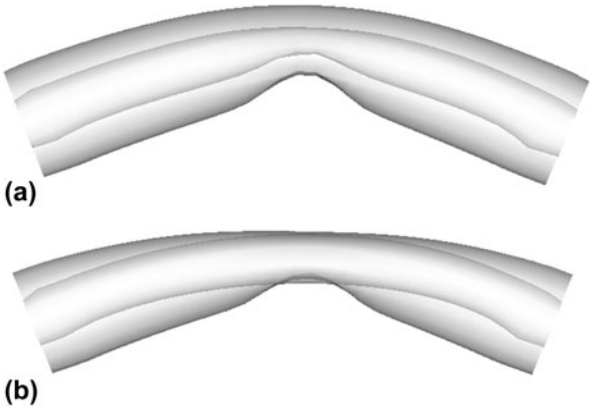


Figure 9: Bending buckling patterns of the (6,0) (13,0) double-walled CNT (a) with involved vdW interactions and (b) without involved vdW interactions at the bending angle of 23°, respectively.

Concluding remarks

In this study, we have built a van der Waals contact-bond model and proposed a higher-order QC method for the study of the contact behaviors of low-dimensional nanoscale carbon structures. This method takes the multi-body and pair interactions of discrete carbon atoms into account. It is, therefore, as accurate as atomistic simulations. The degree of freedom of the carbon atomic components can be reduced reasonably with the usage of a finite number of nodes to replace the discrete atoms. The saving of computational efforts is tremendous and the computational efficiency is as high as that of continuum simulations. In a nutshell, our method has the advantages of atomistic simulations and continuum models, rendering itself suitable for large-scale problems.

Acknowledgments

We gratefully acknowledge the financial support from the National Natural Science Foundation of China (11602101); the Shandong Provincial Natural Science Foundation for Outstanding Youth, China (ZR2018JL004); and the Promotive Research Fund for Excellent Young and Middle-aged Scientists of Shandong Province, China (BS2014SF004).

References

1. **W.B. Choi, E. Bae, D. Kang, S. Chae, B. Cheong, and J. Ko**: Aligned carbon nanotubes for nanoelectronics. *Nanotechnol* **15**, 512 (2004).
2. **K.T. Lau, M. Chipara, H.Y. Ling, and D. Hui**: On the effective elastic moduli of carbon nanotubes for nanocomposite structures. *Composites, Part B* **35**, 95 (2004).
3. **E.B. Barros, A. Jorio, G.G. Samsonidze, R.B. Capaz, A.G. Souza Filho, J. Mendes Filho, G. Dresselhaus, and M.S. Dresselhaus**: Review on the symmetry-related properties of carbon nanotubes. *Phys. Rep.* **431**, 261 (2006).
4. **K.T. Lau, C. Gu, and D. Hui**: A critical review on nanotube and nanotube/nanoclay related polymer composite materials. *Composites, Part B* **37**, 425 (2006).
5. **T.W. Tombler, C. Zhou, L. Alexseyev, J. Kong, H. Dai, L. Liu, C.S. Jayanthi, M. Tang, and S.Y. Wu**: Reversible electromechanical characteristics of carbon nanotubes under local-probe manipulation. *Nature* **405**, 769 (2000).
6. **B. Liu, H. Jiang, H.T. Johnson, and Y. Huang**: The influence of mechanical deformation on the electrical properties of single wall carbon nanotubes. *J. Mech. Phys. Solids* **52**, 1 (2004).
7. **H. Jiang, B. Liu, Y. Huang, and K.C. Hwang**: Thermal expansion of single wall carbon nanotubes. *ASME J. Eng. Mater. Technol.* **126**, 265 (2004).
8. **B.I. Yakobson, C.J. Brabec, and J. Bernholc**: Structural mechanics of carbon nanotubes: From continuum elasticity to atomistic fracture. *J. Comput.-Aided Mater. Des.* **3**, 173 (1996).
9. **B.I. Yakobson, M.P. Campbell, C.J. Brabec, and J. Bernholc**: High strain rate fracture and C-chain unraveling in carbon nanotubes. *Comput. Mater. Sci.* **8**, 341 (1997).
10. **K.M. Liew, X.Q. He, and C.H. Wong**: On the study of elastic and plastic properties of multi-walled carbon nanotubes under axial tension using molecular dynamics simulation. *Acta Mater.* **52**, 2521 (2004).
11. **K.M. Liew, C.H. Wong, X.Q. He, M.J. Tan, and S.A. Meguid**: Nanomechanics of single and multi-walled carbon nanotubes. *Phys. Rev. B* **69**, 115429 (2004).
12. **E. Hernandez, C. Goze, P. Bernier, and A. Rubio**: Elastic properties of C and BxCyNz composite nanotubes. *Phys. Rev. Lett.* **80**, 4502 (1998).
13. **K. Zhang and E.B. Tadmor**: Energy and moiré patterns in 2D bilayers in translation and rotation: A study using an efficient discrete–continuum interlayer potential. *Extreme Mech. Lett.* **14**, 16 (2017).
14. **K. Zhang and E.B. Tadmor**: Structural and electron diffraction scaling of twisted graphene bilayers. *J. Mech. Phys. Solids* **112**, 225 (2018).

https://doi.org/10.1557/jmr.2019.360 Published online by Cambridge University Press

© Materials Research Society 2019

15. **Z.H. Aitken and R. Huang**: Effects of mismatch strain and substrate surface corrugation on morphology of supported monolayer graphene. *J. Appl. Phys.* **107**, 123531 (2010).
16. **K. Zhang and M. Arroyo**: Understanding and strain-engineering wrinkle networks in supported graphene through simulations. *J. Mech. Phys. Solids* **72**, 61 (2014).
17. **N. Hu, K. Nunoya, D. Pan, T. Okabe, and H. Fukunaga**: Prediction of buckling characteristics of carbon nanotubes. *Int. J. Solids Struct.* **44**, 6535 (2007).
18. **B. Liu, Y. Huang, H. Jiang, S. Qu, and K.C. Hwang**: The atomic-scale finite element method. *Comput. Methods Appl. Mech. Eng.* **193**, 1849 (2004).
19. **X.Q. He, S. Kitipornchai, C.M. Wang, and K.M. Liew**: Modeling of van der Waals force for infinitesimal deformation of multi-walled carbon nanotubes treated as cylindrical shells. *Int. J. Solids Struct.* **42**, 6032 (2005).
20. **W.B. Lu, J. Wu, L.Y. Jiang, Y. Huang, K.C. Hwang, and B. Liu**: A cohesive law for multi-wall carbon nanotubes. *Philos. Mag.* **87**, 2221 (2007).
21. **A. Sears and R.C. Batra**: Buckling of multiwalled carbon nanotubes under axial compression. *Phys. Rev. B* **73**, 085410 (2006).
22. **A. Timesli, B. Braikat, M. Jamal, and N. Damil**: Prediction of the critical buckling load of multi-walled carbon nanotubes under axial compression. *C. R. Mec.* **345**, 158 (2017).
23. **X. Guo, J.B. Wang, and H.W. Zhang**: Mechanical properties of single-walled carbon nanotubes based on higher order Cauchy–Born rule. *Int. J. Solids Struct.* **43**, 1276 (2006).
24. **X. Guo, J.B. Liao, and X.Y. Wang**: Investigation of the thermo-mechanical properties of single-walled carbon nanotubes based on the temperature-related higher order Cauchy–Born rule. *Comput. Mater. Sci.* **51**, 445 (2012).
25. **X.Y. Wang and X. Guo**: Numerical simulation for finite deformation of single-walled carbon nanotubes at finite temperature using temperature-related higher order Cauchy–Born rule based quasi-continuum model. *Comput. Mater. Sci.* **55**, 273 (2012).
26. **Y.Z. Sun and K.M. Liew**: The buckling of single-walled carbon nanotubes upon bending: The higher order gradient continuum and mesh-free method. *Comput. Methods Appl. Mech. Eng.* **197**, 3001 (2008).
27. **X.Y. Wang and X. Guo**: Quasi-continuum model for the finite deformation of single-layer graphene sheets based on the temperature-related higher order Cauchy–Born rule. *J. Comput. Theor. Nanosci.* **10**, 154 (2013).
28. **X.Y. Wang, J.B. Wang, and X. Guo**: Finite deformation of single-walled carbon nanocones under axial compression using a temperature-related multiscale quasi-continuum model. *Comput. Mater. Sci.* **114**, 244 (2016).
29. **X.Y. Wang, X. Guo, and Z. Su**: A quasi-continuum model for human erythrocyte membrane based on the higher order Cauchy–Born rule. *Comput. Methods Appl. Mech. Eng.* **268**, 284 (2014).
30. **P. Xiang and K.M. Liew**: Predicting buckling behavior of microtubules based on an atomistic-continuum model. *Int. J. Solids Struct.* **48**, 1730 (2011).
31. **M. Arroyo and T. Belytschko**: An atomistic-based finite deformation membrane for single layer crystalline films. *J. Mech. Phys. Solids* **50**, 1941 (2002).
32. **M. Arroyo and T. Belytschko**: Nonlinear mechanical response and rippling of thick multiwalled carbon nanotubes. *Phys. Rev. Lett.* **91**, 215505 (2003).
33. **M. Arroyo and T. Belytschko**: Finite element methods for the non-linear mechanics of crystalline sheets and nanotubes. *Int. J. Numer. Methods Eng.* **59**, 419 (2004).
34. **X.Y. Wang and X. Guo**: Quasi-continuum contact model for the simulation of severe deformation of single-walled carbon nanotubes at finite temperature. *J. Comput. Theor. Nanosci.* **10**, 810 (2013).
35. **H. Gao and P. Klein**: Numerical simulation of crack growth in an isotropic solid with randomized internal cohesive bonds. *J. Mech. Phys. Solids* **46**, 187 (1998).
36. **S.N. Atluri and T. Zhu**: A new Meshless Local Petrov-Galerkin (MLPG) approach in computational mechanics. *Comput. Mech.* **22**, 117 (1998).
37. **S.N. Atluri and T. Zhu**: A new meshless local Petrov–Galerkin (MLPG) approach to nonlinear problems in computer modeling and simulation. *Comput. Model. Simul. Eng.* **3**, 187 (1998).
38. **D.W. Brenner**: Empirical potential for hydrocarbons for use in simulating the chemical vapor deposition of diamond films. *Phys. Rev. B* **42**, 9458 (1990).
39. **J.E. Lennard-Jones**: The determination of molecular fields: From the variation of the viscosity of a gas with temperature. *Proc. R. Soc.* **106**, 441 (1924).
40. **L.A. Girifalco, M. Hodak, and R.S. Lee**: Carbon nanotubes, buckyballs, ropes, and a universal graphitic potential. *Phys. Rev. B* **62**, 13104 (2000).
41. **P. Lancaster and K. Salkauskas**: Surfaces generated by moving least squares methods. *Math. Comput.* **37**, 141 (1981).
42. **S. Iijima, C. Brabec, A. Maiti, and J. Bernholc**: Structural flexibility of carbon nanotubes. *J. Chem. Phys.* **104**, 2089 (1996).

https://doi.org/10.1557/jmr.2019.360 Published online by Cambridge University Press

© Materials Research Society 2019